Use of proteolytic sequences with different cleavage kinetics as a way to generate hydrogels with preprogrammed cell-infiltration patterns imparted over their given 3D spatial structure

Tatjana Flora[1], I. González de Torre[1, 2], M. Alonso[1], J. Carlos Rodríguez-Cabello[1]

[1] BIOFORGE, CIBER-BBN, Edificio Lucia, Universidad de Valladolid, Paseo Belén 19, 47011, Valladolid, Spain

[2] TECHNICAL PROTEINS NANOBIOTECHNOLOGY (TPNBT S.L.) Paseo Belén 9 A, 47011, Valladolid, Spain

Tatjana Flora
G.I.R BIOFORGE, CIBER-BBN, Universidad de Valladolid
Paseo de Belén 19
47011, Valladolid, Spain
E-mail: tflora@bioforge.uva.es

Dr. Israel Gonzalez de Torre
TECHNICAL PROTEINS NANOBIOTECHNOLOGY (TPNBT S.L.)
Paseo Belén 9 A,
47011, Valladolid, Spain
E-mail: igonzalez@tpnbt.com

Prof. Matilde Alonso
G.I.R BIOFORGE, CIBER-BBN, Universidad de Valladolid
Paseo de Belén 19
47011, Valladolid, Spain
E-mail: malonso@bioforge.uva.es

Prof. José Carlos Rodríguez-Cabello
G.I.R BIOFORGE, CIBER-BBN, Universidad de Valladolid
Paseo de Belén 19
47011, Valladolid, Spain
E-mail: roca@bioforge.uva.es

Abstract.

Control over biodegradation processes is crucial to generate advanced functional structures with a more interactive and efficient role for biomedical applications. Herein, a simple, high-throughput approach is developed based on a 3D-structured system that allows a preprogramed spatial-temporal control over cell infiltration and biodegradation. The 3D-structured system is based on elastin-like recombinamers (ELRs) characterized by differences in the kinetics of their peptide cleavage and consists of a three-layer hydrogel disk comprising an internal layer containing a rapidly degrading component, with the external layers containing a slow-degrading ELR. This structure is intended to invert the conventional pattern of cell infiltration, which goes from the outside to the inside of the implant, to allow an anti-natural process in which infiltration takes place first in the internal layer and later progresses to the outer layers. Time-course *in vivo* studies proved this hypothesis, i.e. that it is possible to drive the infiltration of cells over time in a given 3D-structured implant in a controlled and predesigned way that is able to overcome the natural tendency of conventional cell infiltration. The results obtained herein open up the possibility of applying this concept to more complex systems with multiple biological functions.

1. Introduction

Over the past few years, the application of microfabrication and additive fabrication tools in the biomedical field has produced remarkable advances in the generation of complex structures with well-defined architectures that mimic those found in natural tissues and organs. [1] [2] Currently, the construction of well-defined three-dimensional (3D) structures is one of the most widespread strategies used in regenerative medicine. Indeed, this strategy has led to the construction of complex structures with controlled geometries and with precise control over the composition and spatial distribution. [3, 4] In most cases, these systems are conceived as transient, thus meaning that, once implanted, they either progressively degrade via a chemical process or are digested by the direct action of their cellular cargo or cells recruited from the surrounding tissues. In both cases, the implant is degraded and disappears from the implantation site, with natural tissue replacing the degraded implant. [5] [6]

Fabrication techniques for well-defined 3D structures still face technical challenges in terms of high-resolution cell deposition, controlled cell distributions and vascularization. [7] [8] Apart from these challenges, one evident drawback of current technology is the lack of spatial-temporal control during the degradation process. [8] In general, the well-defined 3D structure of these implants is not related to their degradation process, at least in a controlled manner. Essentially, after implantation, the cells colonize and degrade the implant in an uncontrolled way, thus meaning that the spatial structure and biological function distribution of the implant are not connected with a predefined degradation program. [9] It would therefore be highly desirable for such sophisticated 3D structures to show a linked and programmable degradation sequence as a way of better controlling the evolution of the system once implanted. [10] [11] Currently, control of degradation rate over time is crucial for scaffolds used in tissue-engineering applications and is a key factor influencing the structure and properties of the scaffold. [12] [13] [14]

Elastin-like recombinamers (ELRs) are considered to be advanced biomaterials since they are multifunctional materials that can be tailored to exhibit a wide range of properties as well as functionalities such as cell adhesion, cell signaling, elasticity and biodegradability. [15] [16] [17] Moreover, they can be genetically engineered to exhibit complex biological functionalities as well as stimuli-responsiveness and, more specifically, they can change their physicochemical properties as a result of a change in a given stimulus. [18] [19] These smart biomaterials allow for the emulation of key properties of the natural ECM, specifically the ability to mimic its dynamic changes and complex functionalities. [20] [21] These properties served as a basis and proved essential when choosing the materials to test the hypothesis of this work.

Biomaterial-based implants that include protease recognition moieties in their amino acid composition are one of the most successful approaches towards the generation of functional devices. [22] [23] Proteolysis is one of the first and most sustained cell activities responsible for the structural remodelling and functional plasticity of tissues, which comprise basement membrane degradation, cell migration/ECM invasion, and capillary lumen formation. [24, 25] [26] During these processes, cells migrate and locally secrete a number of enzymes that promote the degradation and remodelling of matrix molecules in their pathway. Matrix metalloproteases (MMPs) and plasmin have been identified as particularly important proteases for cell migration. [27] [28] [29] In particular, the plasminogen activator-plasmin system plays an important role in tissue remodelling and is involved in several pathological processes. Two specific activators and their respective inhibitors, namely tissue plasminogen activator (tPA) and urokinase plasminogen activator (uPA), are mainly responsible for controlling this system. [30] [31] These activators are synthesized by different cell types, such as fibroblasts, epithelial cells, endothelial cells, smooth muscle cells, monocytes/macrophages and tumor cells. Moreover, uPA is actively expressed under circumstances associated with

cell migration (reparation, inflammation, angiogenesis, metastasis), where it provides efficient and spatially restricted extracellular proteolysis. [31, 32] [33]

Recent studies have shown the potential of the creation of 3D microenvironments that behave like actual ECM tissue. These 3D microenvironments can incorporate biological cues, such as protease epitopes, or growth factors to facilitate ECM degradation, cell proliferation, angiogenesis, or regeneration. They can also improve tissue specificity and facilitate maintenance of cell functions and phenotype. [34] [35]

Recently, Straley et al. demonstrated that the kinetics and sensitivity to proteolytic cleavage epitopes of uPA are not the same. Thus, whereas some epitopes, such as GTAR, exhibit a high sensitivity to proteolytic cleavage with a fast response, others, such as DRIR, exhibit a low cleavage efficiency, thus resulting in a delayed proteolytic sensitivity and slower degradation kinetics. [36]

We propose that the differences in peptide cleavage kinetics between those two epitopes can be used to program the degradation and cell-invasion sequence in a given 3D structure. To test this hypothesis, a model 3D structure (a sandwiched three layer disc) was constructed (Figure 1). This was accomplished using ELRs containing both adhesion (RGD sequence) and specific proteolytic sites belonging to the plasminogen activator system (uPA enzyme) but with different degradation rates (fast and slow). The combination of these two types of bioactive signals allowed for the construction of a 3D system with a preprogrammed degradation sequence. This 3D model construct consisted of two external layers formed by a mixture of a proteolytic ELR with a slow degradation rate (DRIR-ELR) and an RGD-ELR, and a central layer composed of a proteolytic ELR with a fast degradation rate (GTAR-ELR) in addition to the RGD-ELR (Figure 1a). In essence, these three layers showed the same physical properties, cell adhesiveness and other biological functions. The concentration of cleavage sites was also the same but the central layer contained the fast degrading GTAR sequence while the two external layers contained the slow degrading DRIR sequence.

The resulting constructs were implanted subcutaneously in mice in order to analyse cell infiltration in a spatial-temporal distribution. (Figure 1b) It is hypothesized that the internal layer will be colonized first following an inside-to-outside pattern rather than the outside-to-inside pattern that is expected in conventional devices without such cell-infiltration programming (Figure 1c-1d).
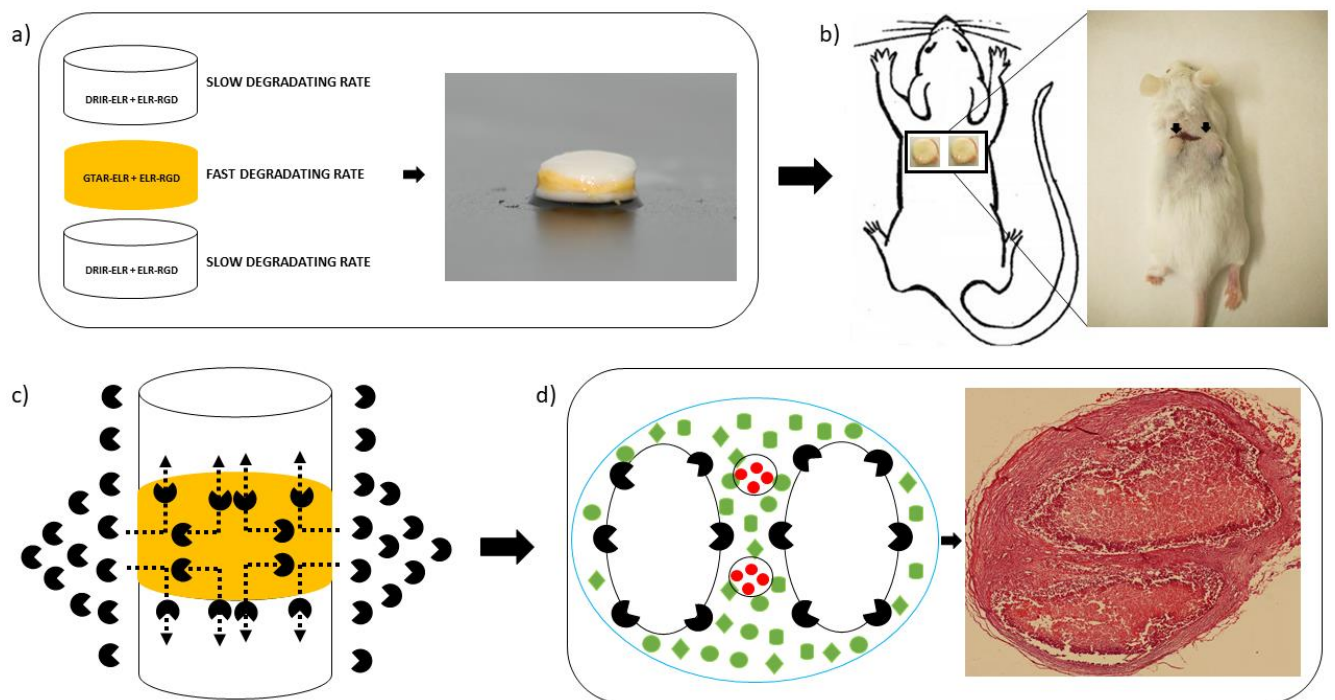

Figure 1. Representation of the 3D-structured system with preprogrammed cell invasion. **a)** A sandwiched three layer disc formed by two external layers (white color) characterized by a slow degradation rate and a central layer (yellow color) characterized by a fast degradation rate. **b)** This 3D structure was implanted subcutaneously into mice. **c)** Cells (the black structures) invaded the central layer of the system first following an outside-to-inside pattern. **d)** At six weeks post-implantation the central layer of the 3D system had been completely degraded, with the consequent formation of functional blood vessels (red circles). The other green structures with different shapes represent other kind of cells that invaded the 3D system. The last image is an H&E stained image showing that the two external layers of the 3D

6

system with the slow degradation rate were not totally degraded, in contrast to the central layer, which was completely degraded.

2. Materials and methods

2.1 Synthesis of GTAR-ELR and DRIR-ELR

All gene-synthesis techniques, biosynthesis and purification protocols have been described in detail elsewhere. [15] [37] [38] The plasmid pUC57 containing the monomer peptides, GTAR and DRIR, was purchased from Nzytech (Lisbon, Portugal). Each monomer was flanked by an NheI recognition site. After extraction from pUC57 plasmid, they were inserted into a previously linearized and dephosphorylated pDrive vector (Qiagen) containing the $(((VPGIG)_2VPGKG(VPGIG)_2)_2$ block. The multi-block sequence was constructed using a directional oligomerization approach called the iterative-recursive method. [39]

A T4 ligase enzyme was used for ligation. This step was repeated four times in order to achieve four repetitions of each gene. Once the genes had been constructed, XL-1 blue component cells were transformed. They were then extracted from the pDrive vector and subcloned into a p7R expression vector which had previously been cut using SapI and dephosphorylated with SAP (Shrink alkaline Phosphatase). Incorporation into the expression vector was confirmed by analytical electrophoresis and subsequent DNA sequencing.

2.2 Expression and characterization of GTAR-ELR and DRIR-ELR

Expression vectors containing GTAR-ELR and DRIR-ELR genes were transformed into BL21 Star (DE3) *E.coli* strain. A screening of the colonies grown overnight (O/N) in auto-induction terrific broth (TB) medium was performed. The inoculum with a concentration of $1.6*10^9$ cells/mL was prepared in Luria-Bertani (LB) medium with ampicillin and glucose and incorporated into the fermenter once it had grown. Production in the fermenter allowed for the use of a higher culture volume and therefore a higher quantity of the desired ELR to be obtained. Bacteria had reached the stationary phase after 15 h, and production was stopped at

17 h. However, bacterial lysis ELRs remained in the soluble fraction afterwards. The ELRs were purified by inverse transition cycling (ITC), which comprises both hot and cold cycles and takes advantage of the smart behaviour of ELRs. The electrophoretic separation of proteins corresponding to the different purification steps, and the final product after purification, were studied in polyacrylamide gels stained with Coomassie Brilliant Blue. In order to ensure the specific features of the final ELR products, physical and chemical characterizations were performed. To that end, SDS-PAGE, MALDI-TOF, nuclear magnetic resonance spectroscopy (NMR), amino acid analysis (HPLC) and differential scanning calorimetry (DSC) techniques were used. (Figure S1-S4, Supporting Information)

2.3 *In vitro* analysis of the degradation rate using a recombinant human uPA enzyme

The degradation rate of GTAR-ELR and DRIR-ELR was studied *in vitro* using a recombinant human uPA enzyme purchased from Hyphen BioMed (Neuville-sur-Oise, France). Each of the recombinamers (100 mM) was incubated with the enzyme at a concentration of 580 U/mL under sterile conditions. Samples were collected at specific time points (0, 15, 30, 60 minutes and 12, 24, 48, 72 hours) and subsequently analysed by SDS-PAGE electrophoresis. For analysis, 20 µL of each sample was mixed with 5 µL of loading buffer and heated at 100 °C for 10 minutes. The degradation rate was monitored on a 15% SDS-PAGE gel stained with Coomassie Brilliant Blue. Each sample was analysed in triplicate.

2.4 Hydrogel formation and physicochemical characterization

Hydrogels were obtained by substituting amine groups at the lateral chain of the lysine residues of each proteolytic ELR with a cyclooctyne group for subsequent crosslinking by a click reaction with RGD-ELR modified with an azide group. Two grams of each proteolytic ELR (DRIR-ELR and GTAR-ELR) was dissolved in 40 mL of dimethylformamide (DMF) at room temperature (RT) for 1 hour. Afterwards, 133.16 mg of Bicyclo [6.1.0] non-4-yn-9-ylmethyl N-succinimidyl carbonate (GalChimia, A Coruña, Spain) dissolved in 1 mL of DMF was added to the solution and the resulting mixture was stirred for 48 h at RT. RGD-ELR was

modified with an azide group as follows. 2-Azido ethyl (2,5-dioxopyrrolidin-1-yl) carbonate (51.69 mg) dissolved in 1 mL of DMF was added to the RGD-ELR solution previously dissolved in DMF as described above. The modified ELRs were purified by washing with 15 mL of diethyl ether and the supernatant was removed and washed with acetone (3 x 15 mL), dried under reduced pressure, re-dissolved in cold MQ water, dialyzed against MQ water and finally lyophilized. Their modification was studied by MALDI-TOF, NMR, FTIR and DSC (Figure S2.1-S2.2, Supporting Information).

2.5 Porosity studies of proteolytic ELR-based hydrogels

The porosity of the hydrogels was determined using the following equation:

$$\text{Porosity (\%)} = \frac{((W_1 - W_2)\,/\,d\,\text{water}) * 100}{V\,\text{hydrogel}} \qquad \textbf{Equation 1}$$

Where W_1 and W_2 are the weight of the swollen and lyophilized gels, respectively, d_{water} is the density of pure water and $V_{hydrogel}$ is the measured volume of the gel in the swollen state. Three replicas were measured for each condition.

2.6 Mechanical properties of proteolytic ELR-based hydrogels

To prepare the proteolytic ELR-based hydrogels, each proteolytic ELR (GTAR-ELR and DRIR-ELR) previously modified with a cyclootyne group was dissolved in PBS 1X at 4°C overnight (O/N). The same conditions were used for dissolution of the RGD-ELR previously modified with an azide group. The concentrations studied were 50, 100 and 150 mg/mL, with a molar ratio of 1:1. For each hydrogel, 50 μL of each proteolytic ELR-cyclootyne was mixed in an Eppendorf flask with 50 μL of RGD-ELR-azide. Subsequently, a specific mold was used to form the hydrogels, which were incubated at 4°C for 20 minutes. Three replicates were analysed for each concentration of each hydrogel. The mechanical properties were studied using a strain-controlled AR-2000ex rheometer (TA Instruments). A stainless steel with a diameter of 12 mm and a gap of about 1000 between the plates was adjusted, reaching a normal force of 0.2 N in order to prevent slippage. All

measurements were conducted at 37°C with a frequency sweep of between 0.01 and 50 Hz at a fixed strain corresponding to the linear hydrogel region.

2.7 Morphological characterization by scanning electron microscopy (SEM)

Hydrogel structure and morphology were evaluated by SEM. After preparation as described above, they were dropped into liquid nitrogen, physically fractured, and immersed in liquid nitrogen again before finally being freeze-dried. Images of lyophilized hydrogels were obtained by SEM (JEOL, JSM-820) with no prior footing procedures. Morphological details such as pore size were evaluated quantitatively using the ZEN (Blue Edition, 2012) software package (Carl Zeiss Microscopy).

2.8 *In vitro* degradation analysis of proteolytic ELR-based hydrogels

The degradation rate of proteolytic ELR-based hydrogels was studied by evaluating the variation of their elastic modulus after incubation with recombinant human uPA enzyme. Hydrogels with a concentration of 50 mg/mL previously prepared in a specific mold were incubated at 37°C with 1 mL of PBS 0.1 M and uPA enzyme at a concentration of 580 U/mL under sterile conditions. Their mechanical properties were analysed using the same approach described in section 2.6.

2.9 Cytocompatibility evaluation in a 2D cell culture

Human umbilical vein endothelial cells (HUVECs) were obtained from the ATCC (Madrid, Spain). Cells were cultured in MED200 medium (Gibco) supplemented with antibiotics gentamicin/amphotericin (1%, Gibco) and low serum growth supplement kit (LSGS, Gibco). They were maintained in a humidified atmosphere containing 5% CO_2 at 37ºC.

The alamarBlue (Invitrogen) bioassay was used to evaluate the cytotoxicity, determining the metabolic activity of HUVECs using a 2D cell culture system consisting of seeding cells on top of the hydrogels. At each time point (4 hours, 3 days, and 7 days), the hydrogels were washed three times with PBS, then 10% alamarBlue in cell culture medium was added to the wells. After each time point, 70 μl of the solutions was transferred into a black, 96-well plate

for fluorescence quantification using a microplate reader. A solution of 10% AB in cell culture medium and a 100% reduced solution of 10% AB in cell culture medium were used as negative and positive control, respectively.

2.10 *In vivo* studies of each proteolytic ELR-based hydrogel

In vivo experiments were performed in accordance with European Union Directive 2010/63/EU and Spanish Royal Decree RD 53/2013. The protocol was approved by the Animal Care and Use Committee of the University of Valladolid. Mice were anesthetized by inhalation using 3% Isoflurane, then 30 µL of each hydrogel, with a concentration of 50 mg/mL, was injected intramuscularly using a syringe with a 20G needle in the hind limb area. Animals were euthanized by cervical dislocation at 3, 6 and 12 weeks.

2.11 Histology and immunohistochemistry analysis

The hydrogels were extracted from the animals at the established time point and were subsequently embedded in 4% paraformaldehyde at 4°C for at least 24 hours. They were then dehydrated in ethanol solutions of increasing concentration (70%, 80%, 90% and 100%); the final step comprised two changes in xylene. All samples were fixed in paraffin for at least 5 hours at 50°C and stored O/N at -20°C. For a general histomorphological evaluation, microsections were cut with a rotatory microtome and stained with hematoxylin and eosin (H&E) according to standard protocols. [40] Three randomly chosen areas of histological staining were selected to perform quantitative analysis using ImageJ.

Immunofluorescence staining was performed on micro-sections previously deparaffinised and subsequently incubated for 1 hour in 10% donkey blocking serum (Santa Cruz Biotechnology, USA). Several washing steps in PBS 1X were then performed. All samples were subsequently incubated overnight (O/N) at 4°C with a goat polyclonal primary PECAM antibody (Santa Cruz Biotechnology, USA) at a concentration of 1 µg/mL in 1% blocking serum. After the primary antibody incubation, samples were washed three times with PBS 1X for five minutes each. Each sample was then incubated for 2 hours with donkey anti-goat (Santa Cruz

Biotechnology, USA) fluorescein-conjugated secondary antibodies at a concentration of 1 µg/mL with 1.5% normal blocking serum. Incubation was carried out with minimal light exposure. After three washes in PBS 1X for five minutes, a vectashield HardSet Antifade Mounting Medium with DAPI (Vector Laboratories, USA) was used to stain the nuclei of the cells. All images were acquired using a fluorescent microscope.

2.12 Preparation of the 3D-structured system

The 3D system consisted of three layers: two external layers formed by DRIR-ELR and RGD-ELR and the central layer formed by GTAR-ELR and RGD-ELR. For the preparation of each system, a specific mold with a diameter of 0.8 mm and a height of 0.4 mm was used. The first step involved depositing the first layer (DRIR-ELR + RGD-ELR) for 2 minutes at 4°C. The second layer (GTAR-ELR + RGD-ELR) was then deposited under the same conditions, and finally the third layer (DRIR-ELR + RGD-ELR) was deposited. The mold containing the entire structure was left for more than 20 minutes at 4°C under sterile conditions.

2.13 *In vivo* studies of the 3D-structured system

The 3D structures were implanted subcutaneously in mice anesthetized using ketamine and diazepam at a concentration of 100 and 5 mg/ml, respectively. A small incision was made on the dorsal area to form a skin pocket using surgical scissors. The entire cylinder (0.8 mm swollen previously in PBS 1X sterile and endotoxin free) was implanted and the wound was closed using absorbable sutures. Different time points were analysed (1, 3, 6, 9 and 12 weeks), with the animals being euthanized by cervical dislocation at each time point. All samples were analysed by histology and immunohistochemistry as described above. Quantitative analysis were performed using Image J software as reported above.

2.14 Statistical analysis

All data are presented as mean ± SD (n = 3). Statistical analysis involved a one-way analysis of variance using the Holm–Sidak method. A *p* value of less than 0.05 was considered to be

statistically significant. (**) $p < 0.001$, (*) $p < 0.05$, and $p > 0.05$. n.s.d indicates no significant differences.

3. Results

3.1 Construction, production and purification of proteolytic ELRs

The amino acid sequences of the resulting proteolytic ELRs (GTAR and DRIR) are shown in Table 1. Each proteolytic ELR comprises a main block $(((VPGIG)_2VPGKG \ (VPGIG)_2)_2$, which is repeated four times, with each cleavage peptide appearing in the middle. The entire DNA sequencing and restriction mapping analysis showed the accuracy of the gene-construction process. (Figure S1)

Purification were carried out using an ITC protocol and the production yields obtained were around 350 mg/L of bacterial culture. The purity, molecular mass and correctness of the biosynthetic process of the final product were confirmed by SDS-PAGE electrophoresis (Figure S2), FTIR (Figure S3), MALDI-TOF mass spectrometry (Figure S4), and amino acid analysis (Table S1).

Table 1. Amino acid sequence of the proteolytic ELRs

Proteolytic ELRs	Amino acid sequence
GTAR	MESLLPV $(((VPGIG)_2 \ VPGKG \ (VPGIG)_2)_2$ YAVTG <u>DRIR</u> SASPASSA $((VPGIG)_2 \ VPGKG \ (VPGIG)_2)_2V)_4$
DRIR	MESLLPV$(((VPGIG)_2 \ VPGKG \ (VPGIG)_2)_2$YAVTG <u>GTAR</u> SASPASSA $((VPGIG)_2 \ VPGKG \ (VPGIG)_2)_2V)_4$

3.2. *In vitro* enzymatic degradation of proteolytic ELRs

The degradation rate of each proteolytic ELR (GTAR-ELR and DRIR-ELR) was studied *in vitro* by SDS-PAGE electrophoresis with Coomassie Brilliant Blue staining. A representative profile of the degradation rate of proteolytic ELRs within a range of time points is shown in Figure 2. At time zero, the molecular weight of the bands corresponding to the recombinamer was about 42 kDa. After 15 minutes, the full protein degraded into smaller fragments with molecular weights of approximately 35, 25, 15 and 5 kDa. The size of these bands

13

corresponds to the theoretical length of the fragments generated upon cleavage at the proteolytic sites. The presence of other fragments that do not correspond to these molecular weights is due to the residual nonspecific cleavage of lysine sites. [41] After 60 minutes, a clear difference was noted between the recombinamer with a fast degradation rate and the recombinamer with a slow degradation rate. Thus, the upper bands of the recombinamer with a fast degradation rate (GTAR-ELR) were absent and the smallest band of 5 kDa increased in intensity. After 12 hours, GTAR-ELR was completely degraded and the only remaining band was that at 5 kDa. The recombinamer with a slow degradation rate did not reach complete degradation over the time period studied. One change that can be noticed for these time points is the loss of intensity in the upper bands, thus meaning that the band corresponding to the full protein began to degrade. These results indicate that there is a clear difference between the ELRs with fast and slow degradation rates and that the degradation rate can be modified using these different cleavage sites.
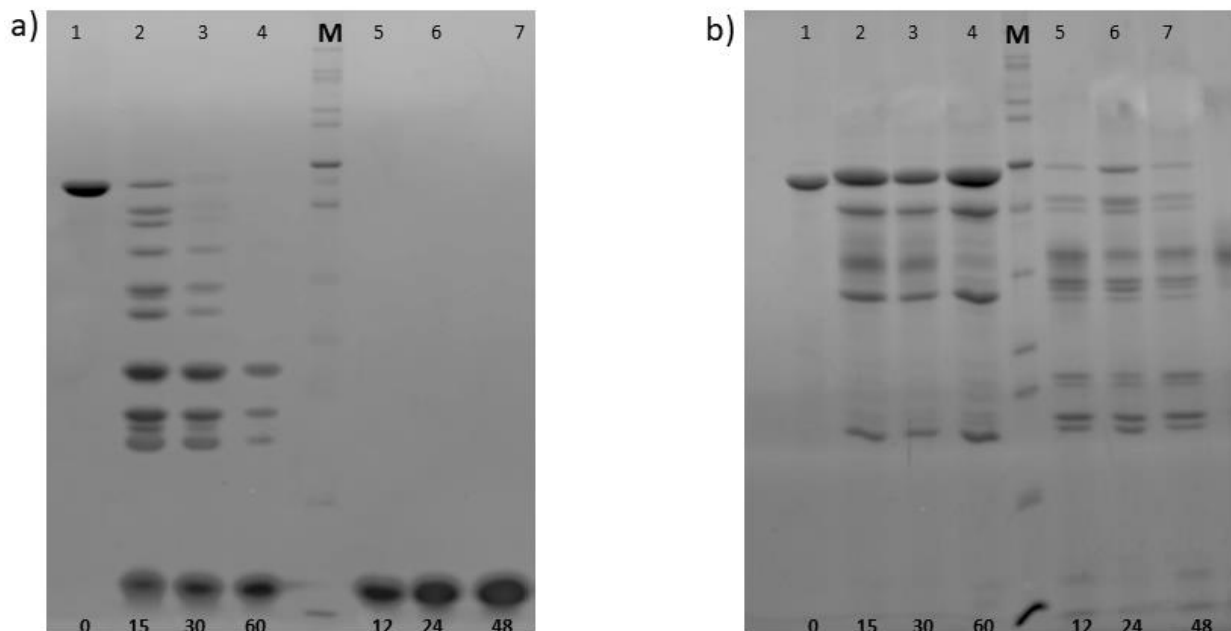
Figure 2. SDS-PAGE electrophoresis of the proteolytic ELRs: a) GTAR-ELR, b) DRIR-ELR. 15% SDS-PAGE stained with Coomassie. In both gels: Lines 1-4: proteolytic ELR

14

degradation after 0, 15, 30 and 60 minutes. Line M: Page Ruler unstained Protein Ladder. Lines 5-7: protein degradation after 12, 24, and 48 hours.

3.3 Morphology studies of proteolytic ELR-based hydrogels

The morphology of the proteolytic ELR-based hydrogels at several concentrations in a frozen-lyophilized state was analysed by SEM microscopy. SEM micrographs of GTAR-ELR and DRIR-ELR hydrogels at several concentrations (50, 100 and 150 mg/mL) can be found in Figure 3a and 3b, respectively. It is evident that the dried porosity decreases with increasing concentration. In hydrogels with a concentration of 100-150 mg/mL, the shape of the pores is irregular and some zones are characterized by a non-pore size. It is also clear that their structure converts into a denser and tighter structure formed by smaller pores. The hydrogels with a concentration of 150 mg/mL present a collapsed network, thus leading to a shrunken state. There is an inverse correlation between concentration and pore size, which further affects the swelling ratio. Hydrogels with a concentration of 50 mg/mL display a higher number of pores with a regular and ordered porosity and also maintain high interconnectivity. A quantitative analysis of the pore size was performed using the ImageJ software, giving a range of about 13 µm. The microscopic structure of the proteolytic ELR-based hydrogels was studied in more detail in order to determine the porosity values, which are reported graphically in Figure 3c. The porosity of the hydrogels was evaluated as a function of concentration, demonstrating that porosity decreases with increasing concentration. These results are in agreement with the SEM analysis. Moreover, both ELR-based hydrogels (GTAR-ELR and DRIR-ELR) exhibit similar morphological features at a concentration of 50 mg/mL.
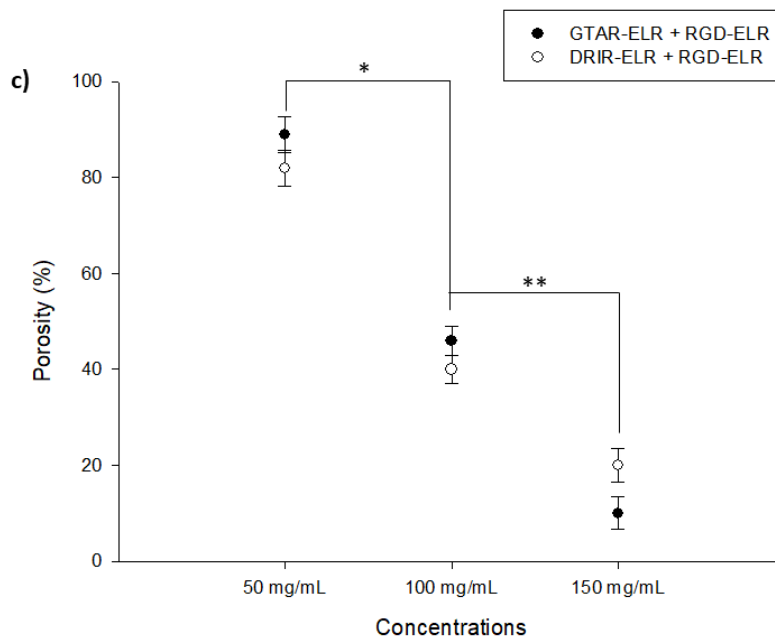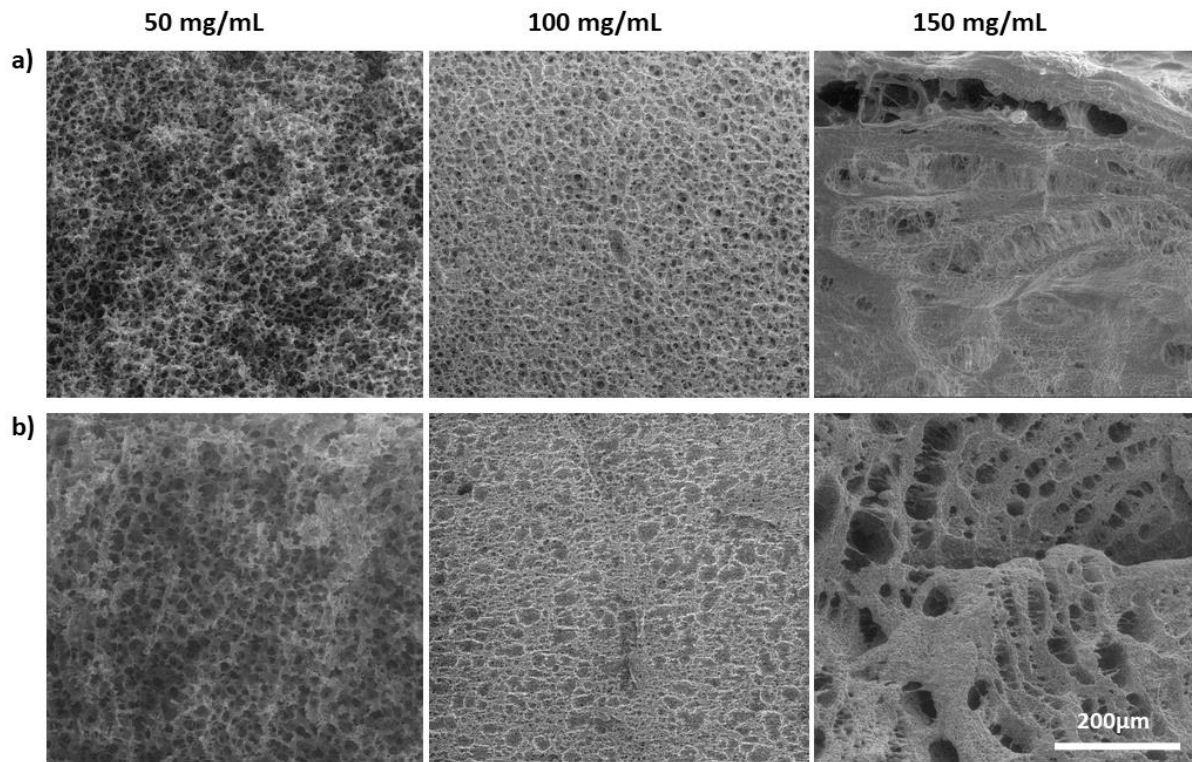
Figure 3. SEM micrographs of cryo-fractured proteolytic ELR-based hydrogels: a) GTAR-ELR + RGD-ELR based hydrogels at 50, 100 and 150 mg/mL from left to right; b) DRIR-ELR + RGD-ELR based hydrogels at 50, 100 and 150 mg/mL. Scale bar for all images: 200µm. c) Graphical representation of porosity versus concentration. Data are reported as

mean ± SD. Statistical analysis involved analysis of variance using the Holm–Sidak method. *p<0.05; **p<0.001.

3.4 Mechanical properties of proteolytic hydrogels

The mechanical properties of the hydrogels were determined by rheological measurement in oscillatory mode. Each hydrogel sample was used for only one test and each test was performed in triplicate. All rheological tests were performed at 1% strain as a previous measurement to demonstrate that the strain amplitude remained constant at 7-8%. The complex elastic modulus reported in Figure 4 represents the average of three tests performed at 37°C, together with the corresponding standard deviation. As reported above, the complex elastic modulus of the hydrogels increased as a function of concentration to 1085±145, 2132±192 and 5253±248 Pa for 50, 100 and 150 mg/mL, respectively, at a frequency of 1 Hz. A statistically significant difference was found between the complex moduli of the hydrogels belonging to the different concentration groups, whereas relatively similar values, with no significant difference in complex modulus, were found for a given concentration for different proteolytic ELR-based hydrogels. The morphological analysis, mechanical properties and swelling ratios demostrated that hydrogels with a concentration of 50 mg/mL exhibit similar properties to that for the scaffold used to regenerate soft tissues.[42] Moreover, the different cleavage site does not appear to affect their mechanical and morphological properties. [8, 43]
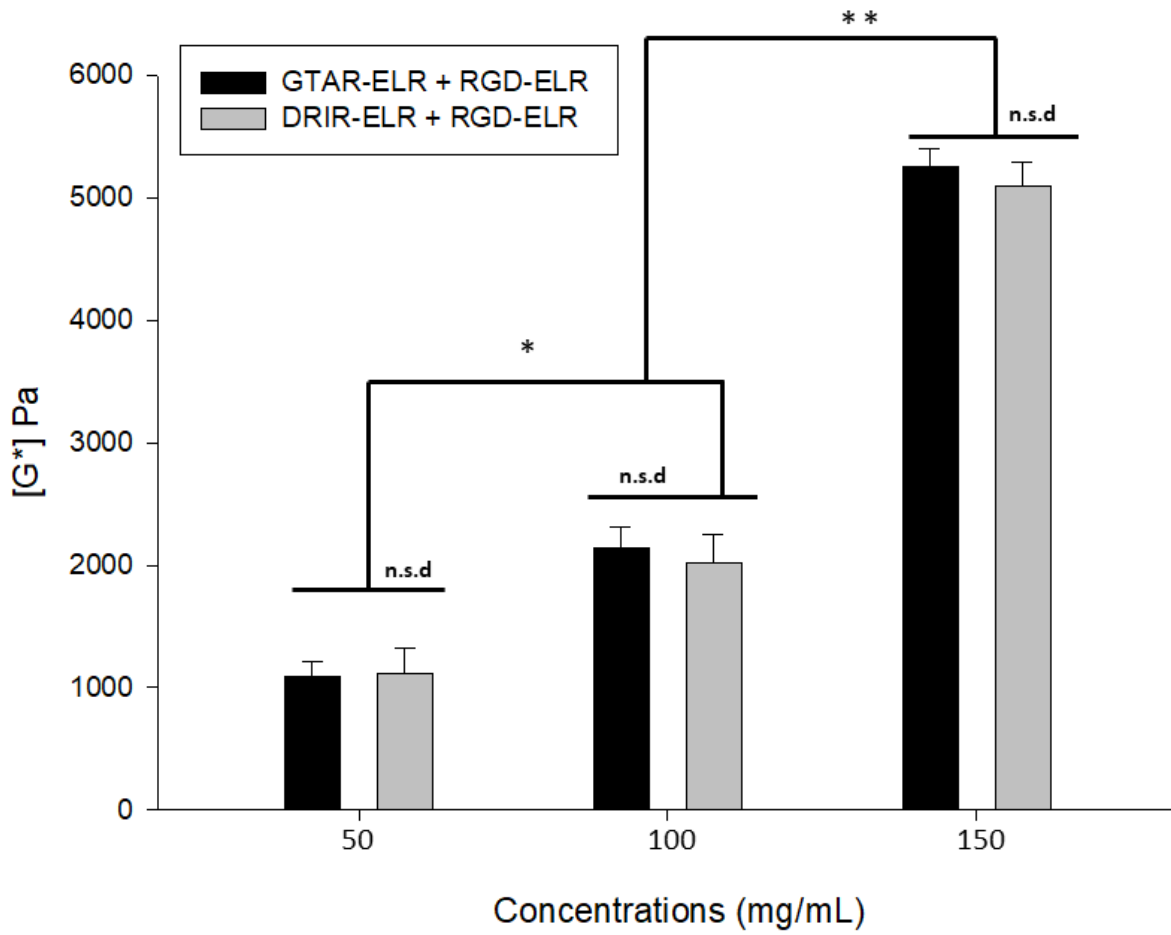
Figure 4. Representation of the complex modulus [G*] for GTAR-ELR + RGD-ELR and DRIR-ELR + RGD-ELR hydrogels at different concentrations. Data are reported as mean ± SD (n=3). Statistical analysis involved analysis of variance using the Holm–Sidak method. *$p<0.05$; **$p<0.001$; n.d.s. no significant differences.

3.5 Degradation rate of the proteolytic ELR-based hydrogels evaluated by analysing the mechanical properties

The degradation rate of the hydrogels was assessed by monitoring the variation of the elastic modulus for 24, 48, 72 and 168 hours. Rheological measurements were performed in oscillatory mode, as described above. The resulting complex modulus was compared to the measurements at time 0 in order to determine the variation in their magnitude after incubation with the corresponding concentration of uPA enzyme. As can be seen from Figure 5, the

complex modulus [G*] at time 0 for the hydrogels with a concentration of 50 mg/mL was about 1100 Pa. After 24 hours, the complex modulus of the hydrogels with a fast degradation rate (GTAR-ELR + RGD-ELR) had decreased by nearly half, whereas the modulus of the hydrogels with a slow degradation rate (DRIR-ELR + RGD-ELR) remained unaffected. This behaviour was expected for the hydrogels with a fast degradation rate (GTAR-ELR + RGD-ELR) since the enzyme had cleaved the majority of the proteolytic sites. However, an interesting phenomenon was observed after 48 hours. Thus, the complex modulus of the hydrogels with a slow degradation rate (DRIR-ELR + RGD-ELR) decreased significantly whereas the modulus for the hydrogels with a fast degradation rate (GTAR-ELR + RGD-ELR) decreased only slightly. After 72 hours, the complex modulus of the hydrogels with a fast degradation rate (GTAR-ELR+ RGD-ELR) was impossible to measure due to their loss of integrity. As such, the last two points for the measurements are not shown in the graph reported in Figure 5. As regards the hydrogels with a slow degradation rate (DRIR-ELR + RGD-ELR), the complex modulus started to slowly decrease, reaching a complex modulus of 676 ± 62 Pa after 168 hours.
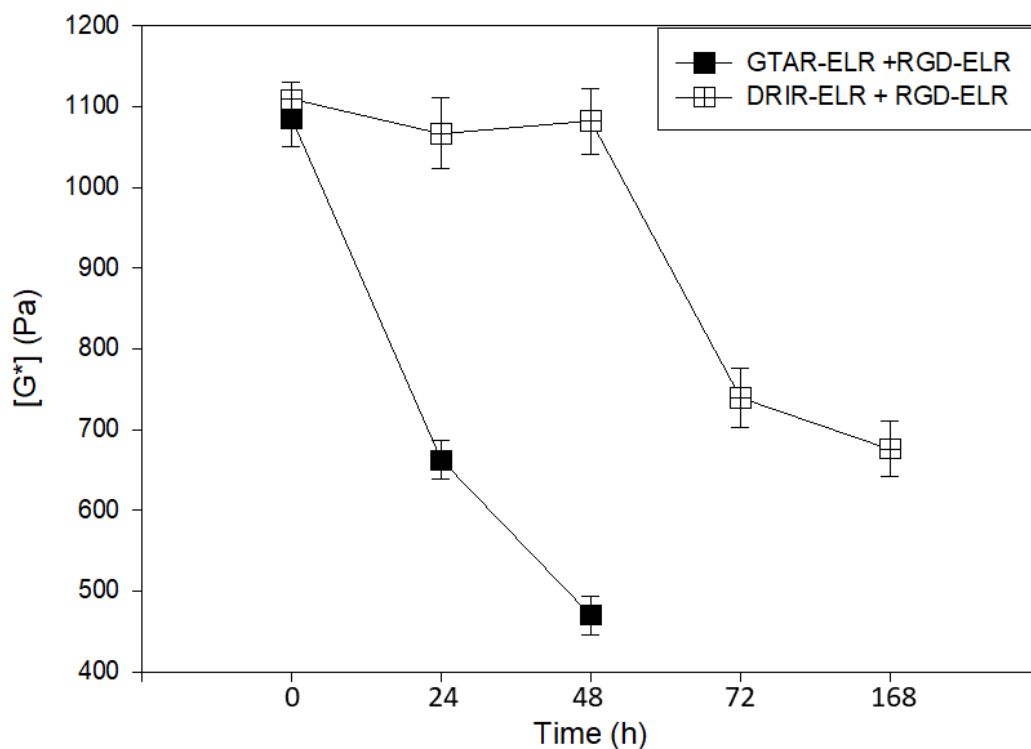
Figure 5. Graphical representation of the complex elastic modulus [G*] for the proteolytic ELR-based hydrogels after exposure to the uPA recombinant human enzyme at 0, 24, 48, 72 and 168 hours. It was not possible to measure the elastic modulus of the last two time points for hydrogels with a fast degradation rate (GTAR-ELR + RGD-ELR). Data are reported as mean ± SD.

3.6 Cytocompatibility

The cytocompatibility of the hydrogels was evaluated using an alamarBlue bioassay considering three time points (4 hours, 3 days and 7 days). A representative graph is provided in Figure 6, where the cell number is reported for each hydrogel at each time-point. The metabolic activity assay revealed that hydrogels promote adherence and proliferation of HUVEC cells. After 4 hours, the endothelial cells adhered similarly in all the hydrogels, and at days 3 and 7 the cell metabolic activity increased, thus demonstrating that these hydrogels support cell growth and proliferation and confirming their cytocompatibility.
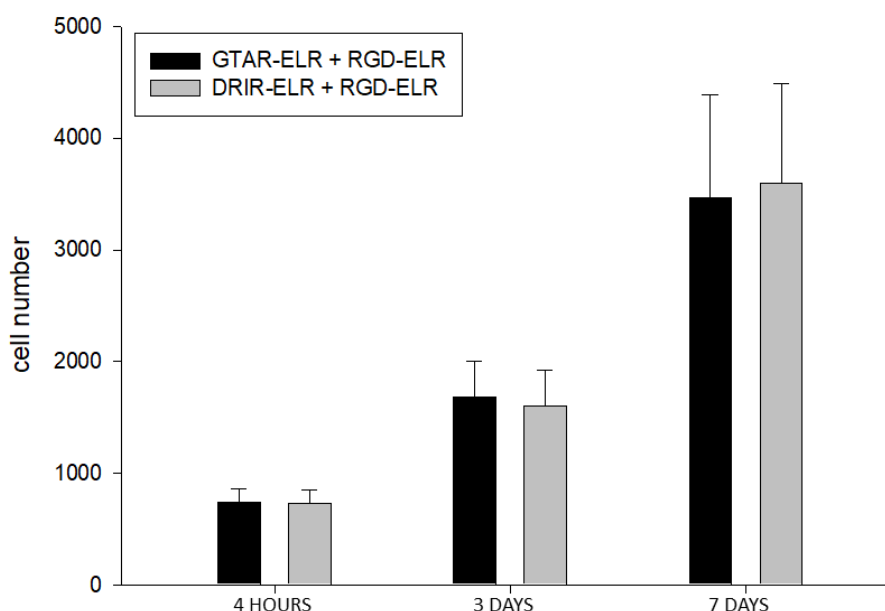

Figure 6. Cytocompatibility evaluation (adhesion and proliferation of endothelial cells) of proteolytic ELRs-based hydrogels using the alamarBlue assay. Error bars represent mean ± SD.

20

**3.7 Individual *in vivo* behaviour of proteolytic ELR-based hydrogels**

In this section, we investigate the *in vivo* behaviour of proteolytic ELR-based hydrogels in order to offering a general overview regarding their degradation rate based on the different cell invasion behaviours exhibited by them. Thus, the hydrogels were injected intramuscularly into mice using a syringe containing a solution of a specific proteolytic ELR and RGD-ELR previously mixed in an eppendorf.

The proteolytic ELR-based hydrogels integrated within the surrounding host tissue, although the tissue response after injection was distinct for the hydrogels with a fast degradation rate (GTAR-ELR + RGD-ELR) and those with a slow degradation rate (DRIR-ELR + RGD-ELR). A hydrogel comprising RGD-ELR and VKV-ELR was used as a control. VKV-ELR is a recombinamer that does not contain any proteolytic sites. As reported in Figure 7a (the first row), after three weeks post-injection, all hydrogels remained at the injection site and start to be invaded by cells. A graphic representation reported in Figure 7b show significant differences in cell number/mm^2 among the samples analysed, especially hydrogels with a fast degradation rate (GTAR-ELR+RGD-ELR) contained a higher number of cells compared to the other systems tested. On the other hand, the hydrogels with a slow degradation rate (DRIR-ELR+RGD-ELR) presented a higher number of cells rather than the control (VKV-ELR+RGD-ELR), which contained regions that were not invaded by any cells. In addition, cells migrated more deeply into the hydrogels with a fast degradation rate (GTAR-ELR+RGD-ELR) than into those with a slow degradation rate (DRIR-ELR+RGD-ELR), almost certainly as a consequence of their degradation rate. We hypothesize that the cells colonizing the hydrogels were a heterogeneous population of cells characteristic of the acute inflammatory response, which is a peripheral reaction during inflammatory infiltration. These results offer an insight into how the different degradation rates influence cell migration into the hydrogels, thereby resulting in a marked variation in cell   density.

An interesting event occurred at six weeks post-injection (second row in Figure 7). As regards the hydrogels with a fast degradation rate (GTAR-ELR+RGD-ELR), these were found to be completely invaded by cells and the formation of small capillaries was observed. In hydrogels with a slow degradation rate (DRIR-ELR+RGD-ELR) cells migrated deeper, although some areas were not invaded completely. An initial inflammatory response starts which is characterized by the presence of macrophages that invaded the hydrogels and started to concentrate around the individual hydrogels. (Figure S3.2, Supporting Information) However, this inflammatory response was reduced or completely disappeared at the following time point. As the degradation process proceeded, a larger number of cells reached deeper within the proteolytic hydrogels, thus accelerating their degradation and leading to destruction of their structure. (Figure 7c) Moreover, the quantity of cells that invaded the control hydrogel was low due to the difficulty encountered by the cells when invading the hydrogel due to the lack of proteolytic sites.

At twelve weeks post-injection signs of degradation became more evident for both proteolytic hydrogels, especially their surface area which decreased considerably. At three weeks the area of all the hydrogels was about 1.01 mm^2. After twelve weeks post-injection the remaining area was about 0.89 mm^2 for VKV-ELR+RGD-ELR, 0.30 mm^2 for GTAR-ELR+RGD-ELR and 0.63 mm^2 for DRIR-ELR+RGD-ELR. Degradation appeared to be more advanced in hydrogels with a fast degradation rate (GTAR-ELR+RGD-ELR), probably indicating resorption of the biomaterial. In summary, at six weeks post-injection, the hydrogels started to lose their internal structural integrity as the rate of hydrogel degradation was accelerated, thus resulting in a noticeably decrease in the volume of the injected hydrogel at twelve weeks post-injection.

Additionally, in hydrogels with a slow degradation rate (DRIR-ELR+RGD-ELR) very few macrophages were present around the remaining sample whilst in hydrogels with a fast degradation rate (GTAR-ELR+RGD-ELR), the inflammatory cells were no longer present.

Moreover, in hydrogels with a slow degradation rate vascularization increased compared to the previous interval. (Figure S 3.1) Endothelial cells were found to be localized around the newly formed capillaries, thus contributing to their luminal structure. (third row of Figure 7a) The formation of neo-vascularization was confirmed by immunohistochemical staining using an antibody against the PECAM protein. The presence of cells positive for CD31 antigen was observed for hydrogels with a fast degradation rate at six weeks post-injection (Figure 8a), and for hydrogels with a slow degradation rate at twelve weeks post-injection (Figure 8b).
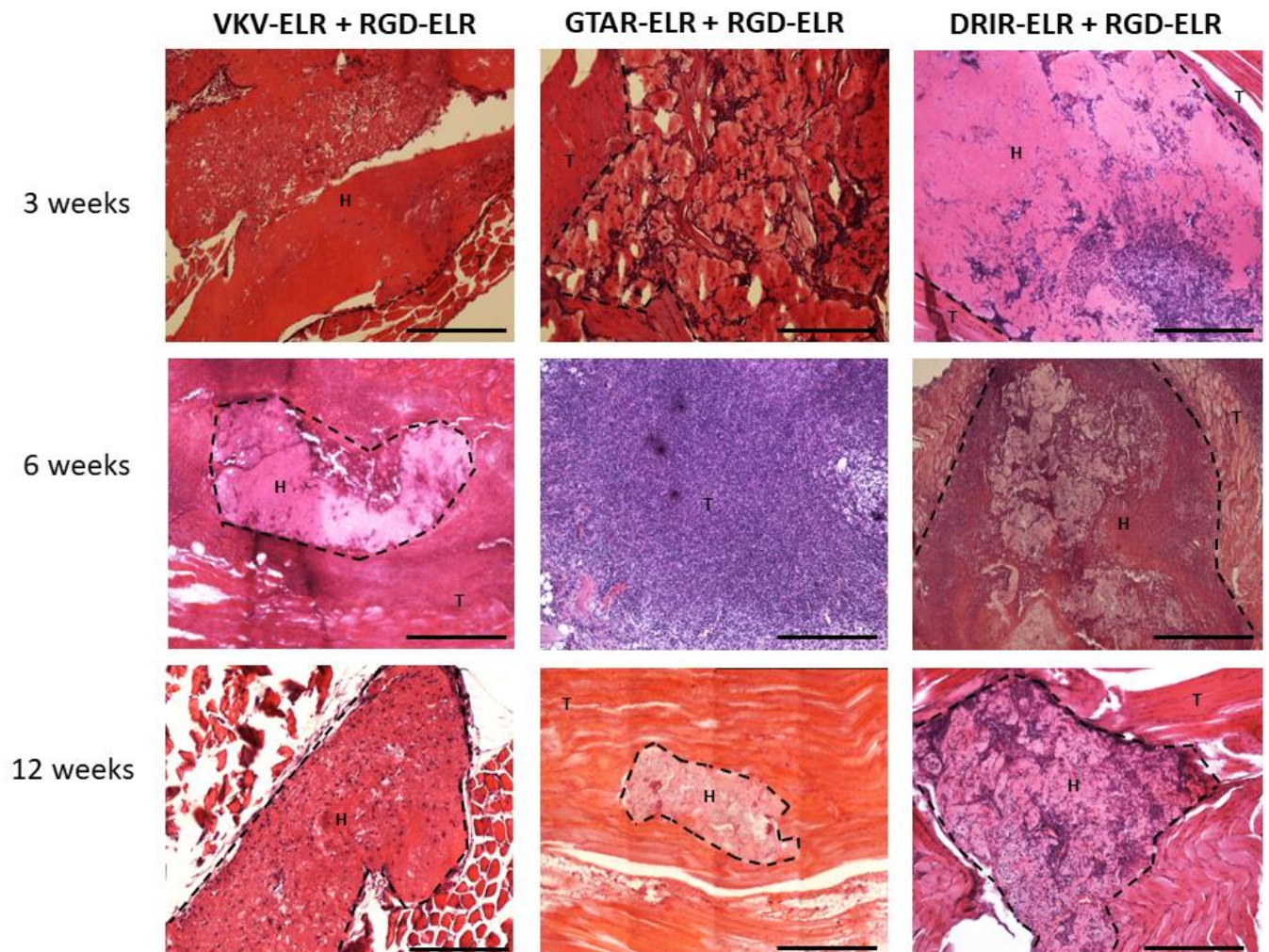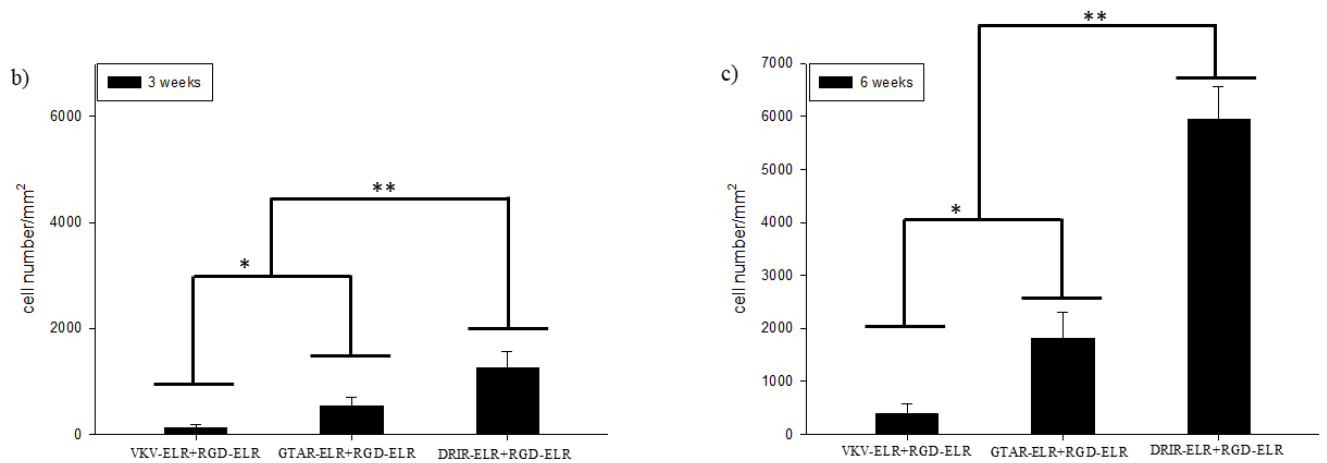
Figure 7. a) Histological hematoxylin and eosin (H&E) staining results for ELR-based hydrogels at 3, 6, and 12 weeks post-injection. The top row indicates the type of sample analysed and the left column indicates the different time points analysed. T: tissue. H: hydrogel. The dotted line represents the interface between tissue (muscle) and hydrogel. Scale bar: 200 µm. b) Graphic representation of number of cells/mm^2 for the hydrogels at three weeks post-injection and c) at six weeks post injection. Each data point represents the mean number of cells, and the bar represents the standard deviation. *$p<0.05$; **$p<0.001$.
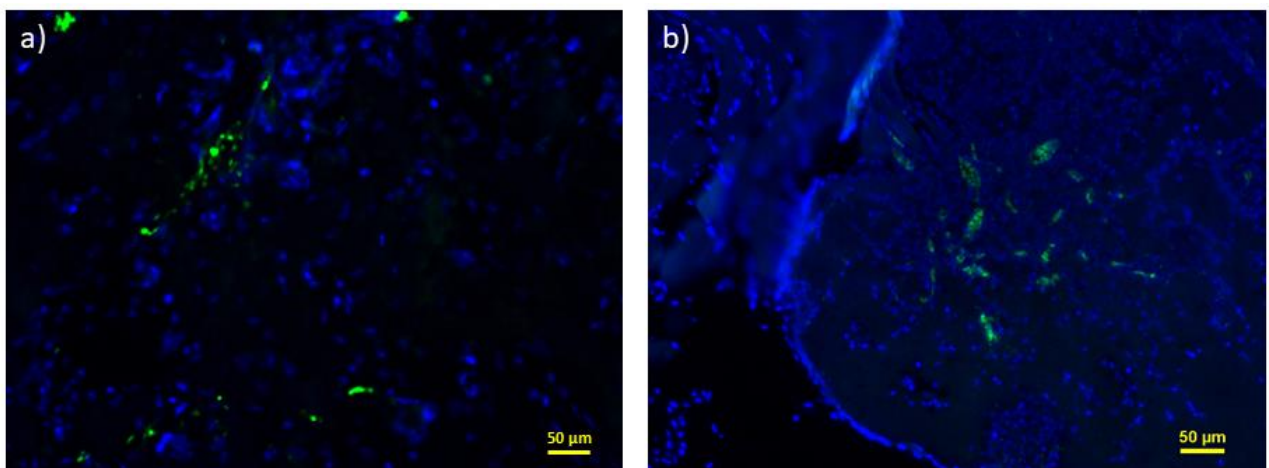
Figure 8. CD31 immunofluorescence staining images of: a) GTAR-ELR+RGD-ELR hydrogel at 6 weeks post-injection; b) DRIR-ELR+RGD-ELR hydrogel at 12 weeks post-injection. DAPI: nucleus staining (blue colour). CD31 protein (green colour). Scale bar: 50 µm.

3.8 *In vivo* studies of the sandwiched three-layer system

After the *in vivo* degradation studies of the individual proteolytic hydrogels, a three-dimensional system mainly comprising a three-layer disc was constructed. This three-layer disc comprised two external layers made of DRIR-ELR+RGD-ELR, characterized by a slow degradation rate, and a central layer made of GTAR-ELR+RGD-ELR, characterized by a fast degradation rate. These discs were implanted subcutaneously in mice and were explanted after 1, 3, 6, 9 and 12 weeks to evaluate the time-course of cell infiltration.

Histological examination upon staining with H&E at each time point is shown in Figure 9. As can clearly be seen (Figure 9a - 9a1), the three parts of the 3D structure can be easily recognized at one week post-implantation. Cell infiltration has not started yet.

At three weeks post-implantation, (Figure 9b - 9b1), a considerable part of the 3D structure was colonized by cells. As predicted, cell infiltration started in the central part of the 3D structure, specifically the layer characterized by a fast degradation rate (GTAR-ELR+RGD-ELR). Figure 9f shows the quantification of cell number/mm^2 that started to invade the central layer of the 3D structure and the cells that infiltrate the edges of the two external layers. There is a significant difference between the quantities of cells that invade the layers of the 3D system.

At six weeks, the central layer of the 3D system was completely invaded by cells and almost completely degraded (Figure 9c – 9c1), and a difference in the degradation rate was clearly observed at this time point. Thus, the external layer of the 3D structure was still not degraded, and the quantity of the cells that invaded these layers clearly increased even if there are significant differences between the quantity of cells that invade the central layer of the 3D system and the two external layers. (Figure 9g)

Moreover, at this time point neovascularization was underway as confirmed in Figure 10 a-b-c where is reported the whole central layer of the 3D system. The blotted circles indicates the presence of blood vessels or capillaries formed. In some of these structures is possible to

detect the presence of endothelial cells surrounding the red blood cells, thereby suggesting the presence of a functional vasculature. (Figure a1, b1, c1) Immunofluorescent staining analysis for a well-known endothelial marker (CD31) was performed. A considerable amount of CD31-positive cells were detected in the central layer of the 3D system (Figure 10d) demonstrating a highly vascularized structure and confirming the presence of blood vessel (Figure 10 d1) that favour the transport of nutrients between the 3D structure and the host tissue. It is evident that the two external parts of the 3D system have no vascularization yet.

At nine weeks post-implantation, the external layers of the 3D structure were almost completely degraded (Figure 9d – 9d1). Although some remnants of the hydrogels remained, they were completely invaded by cells.

The final time point was at 12 weeks. The animals were sacrificed at this point, and no hydrogels remained in the area where they were implanted. Given our previous findings, this allowed us to hypothesize that the entire system had been completely reabsorbed. A summary of the degradation process of the 3D structure when implanted subcutaneously, and how the size thereof changes with time up to the final time point, is provided in Figure 11. At the first three time points the three-layer disc is clearly visible under the skin, thus indicating that it had yet no degraded substantially, and there are no, or very few, macroscopic signs of inflammation or toxicity in the tissue surrounding the implant.
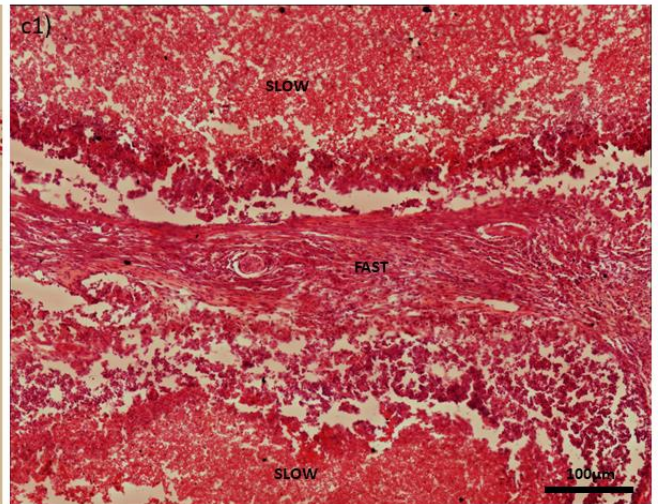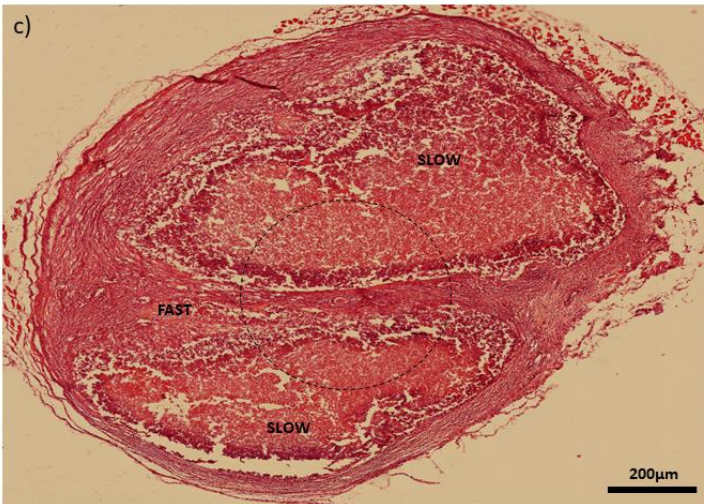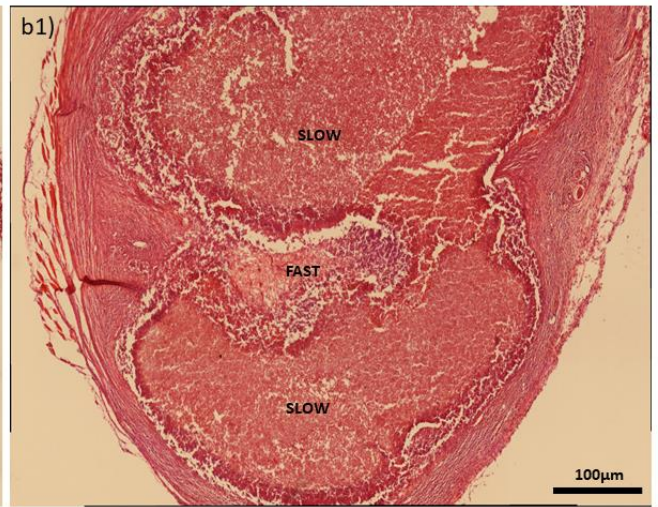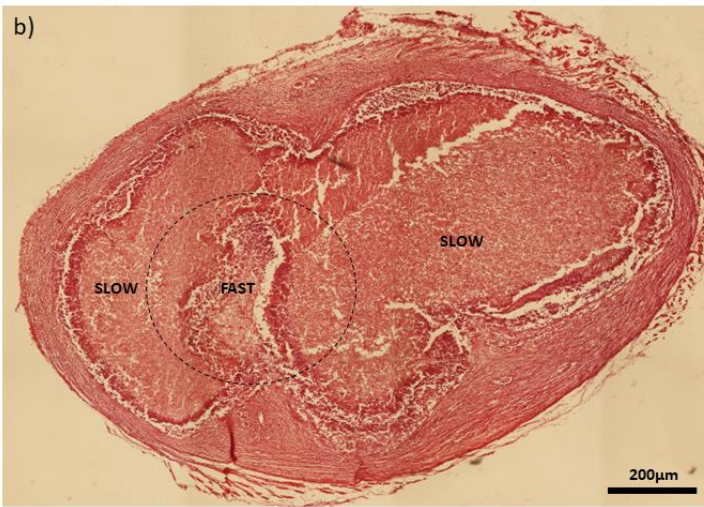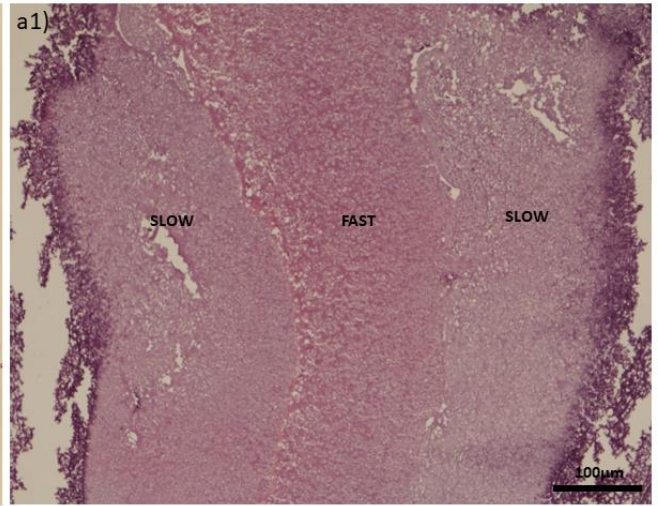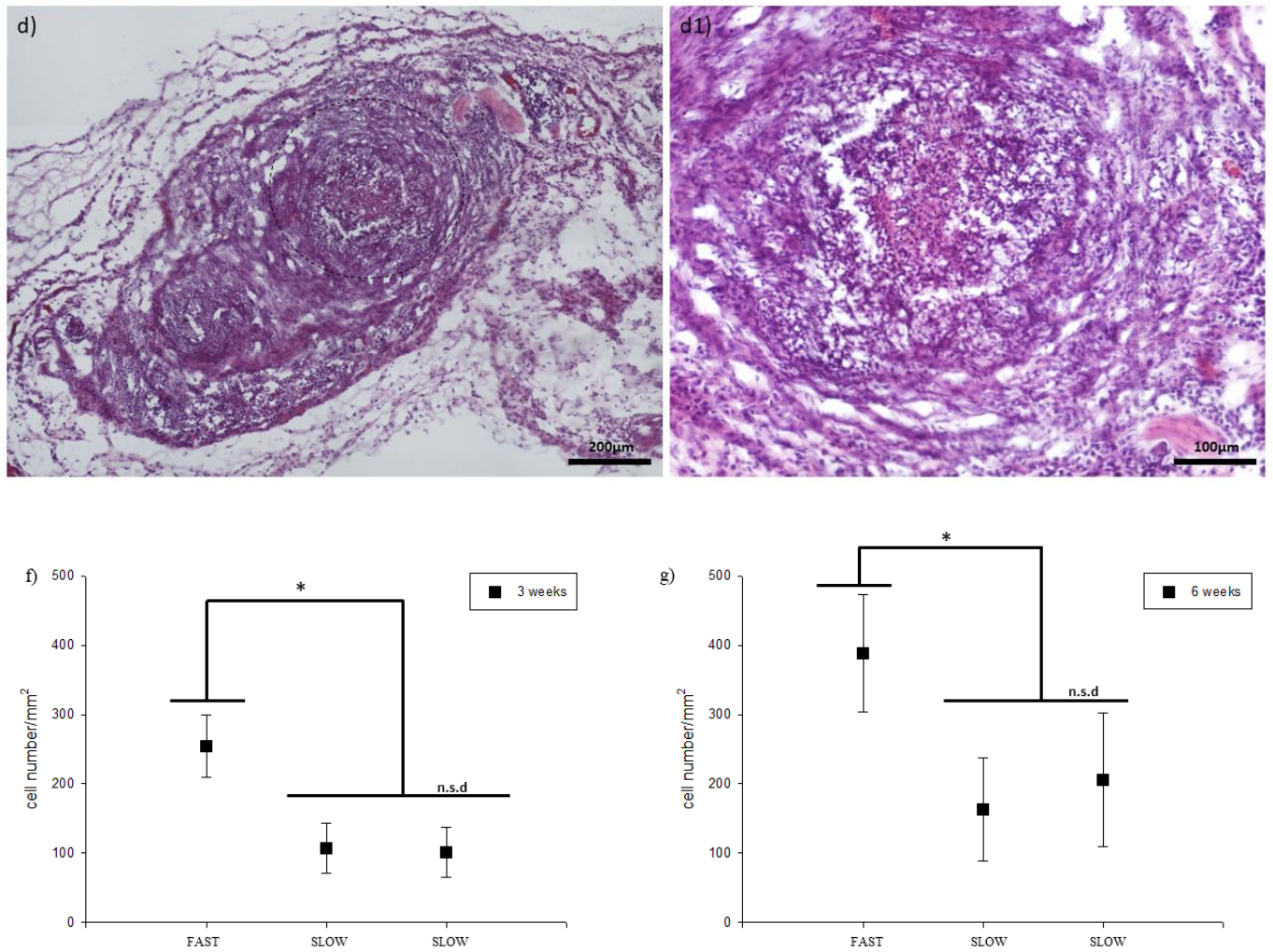
Figure 9. Histological analysis with H&E staining of the 3D structure at: a) 1 week post-implantation, a2) magnification of image where the three parts of the 3D system can be recognized a; b) 3 weeks post-implantation, b1) magnification of image b where it can be observed the initial phase of cell invasion; c) 6 weeks post-implantation, c1) magnification of image c where it can be noticed the complete degradation of the central part of the 3D system; d) 9 weeks post-implantation, d1) magnification of image d where it can be observed the complete cellular invasion and almost complete degradation of the two external parts of the 3D system. The dotted circle indicates the part of the image which was magnified f) graphic representation of number of cells/mm^2 that invaded the three parts of the 3D system after three weeks post-implantation and g) after six weeks post-implantation. Data are reported as mean ± SD. *$p < 0.05$; n.s.d no significant differences.
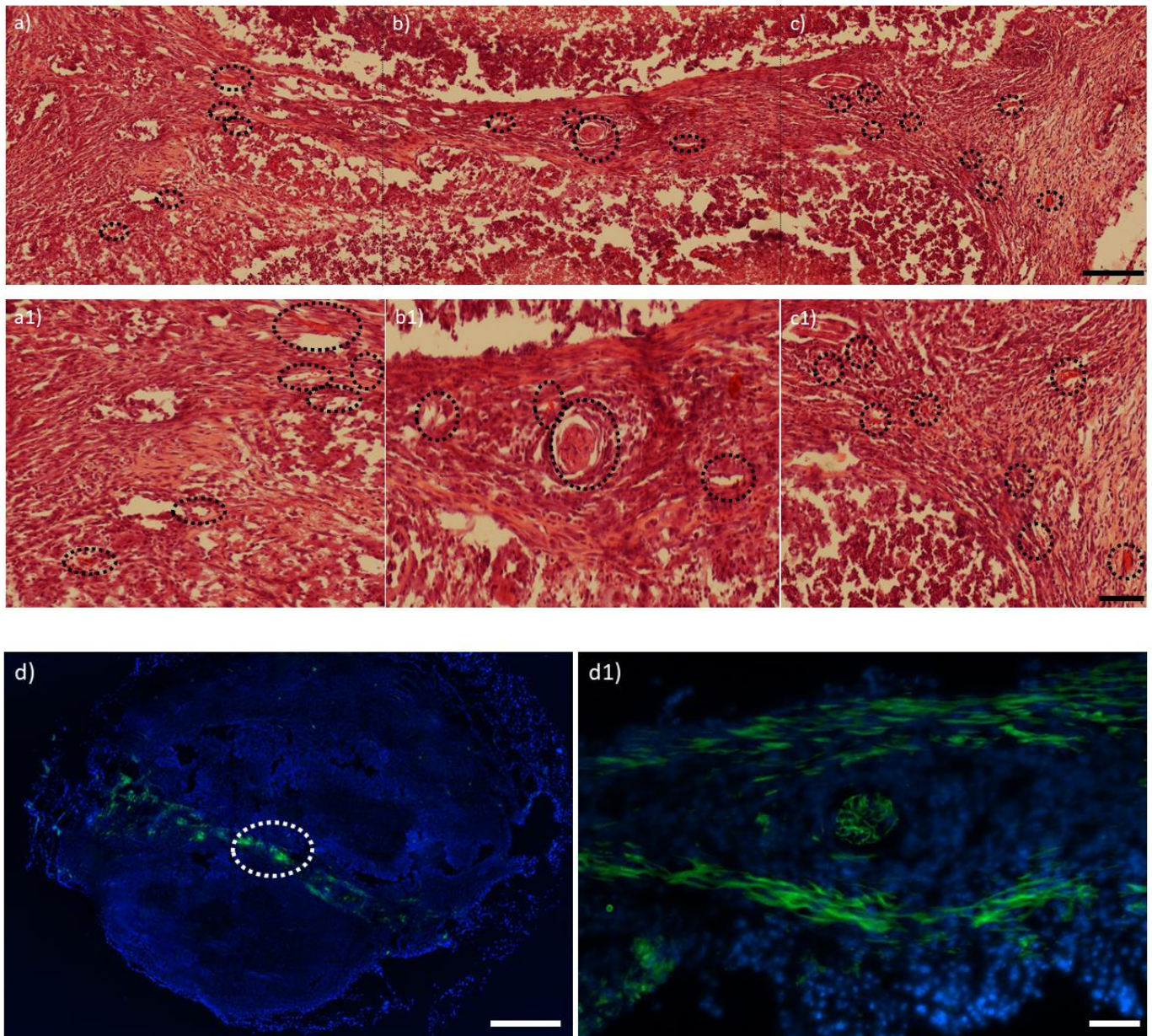
Figure 10. Histological analysis with: (a, b, c) H&E staining of the central part of the 3D-structured system at six weeks post-implantation. a1) magnification of zone a b1) magnification of zone b c1) magnification of zone c. Blotted circles indicates the presence of blood vessels or capillaries. d) CD31 immunofluorescent stain of the whole 3D system. Blotted circle indicates the area magnified in d1) magnification of the central area of the 3D system. Nuclei are stained blue with DAPI and overlaid with green-CD31. Scale bars: a, b, c, d) 100 μm; a1, b1, c1, d1) 50 μm.
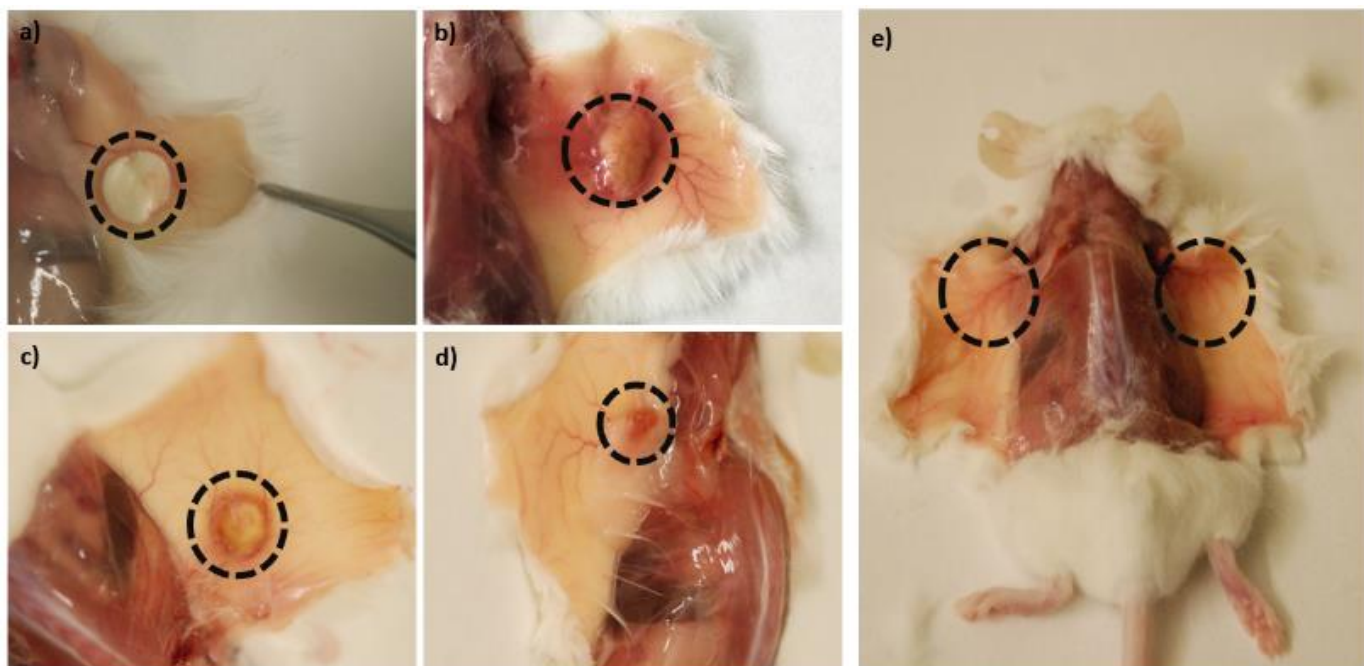
Figure 11. Summary of the 3D structure implantation in mice. The circles indicate the location of the 3D structure after: a) 1 week; b) 3 weeks; c) 6 weeks; d) 9 weeks post-implantation; and e) the complete absence of hydrogels after 12 weeks.

4. Discussion

Control of the biodegradation rate of biological substitutes remains a significant challenge in biomedical applications as a balance between neo-tissue formation and scaffold biodegradation must be achieved. [44, 45] Biomaterials with a controlled and predictable biodegradation are therefore in high demand for the development of multi-functional scaffolds that can simultaneously provide mechanical support, reply to biological signals and resist physiological loads during the early stages of implementation. [46-48] Protease-mediated degradation of biomaterials currently plays an important role in the development of 3D-structured systems employed in tissue engineering as it is able to provide a more precise and controlled environment for pre-programmed cell infiltration and biodegradation. [1] [49]

The 3D system presented herein consists of a bioactive 3D-structured ELR-based hydrogel that provides an appropriate microenvironment for cell growth and proliferation. In particular,

this approach consists of controlling the orientation of cell infiltration over time while also controlling its structural transformation, thus meaning that it can be applied as a temporary soft tissue support for optimal regeneration processes.

This goal was achieved by synthesizing two different ELRs bearing proteolytic target sites with different degradation rates (fast and slow) belonging to the plasminogen activator system, specifically to the uPA enzyme, encoded into their backbone. Furthermore, for the construction of a 3D structure-system, an ELR containing a universal cell-adhesion sequence (RGD) was employed, thereby resulting in the recruitment of a large number of cells inside the hydrogel that can trigger enzymes, thereby inducing proteolysis at the protease-sensitive sites.

With regard to their physicochemical characterization (morphological features, mechanical properties and cytocompatibility), these ELR-based hydrogels proved to be effective as biological substitutes for future applications in tissue engineering. [50-52] [53] [54]

The degradation rate of these systems was initially studied *in vitro* using a human recombinant uPA enzyme, with a clear difference in terms of degradation being found. Initially, the ELR-based hydrogels containing each proteolytic ELR and RDG-ELR were investigated *in vivo* independently in order to determine how their degradation rates influence cell invasion and biodegradation. This study showed that there was a clear difference between the hydrogels containing the ELR with a fast degradation rate and the ELR-based hydrogels with a slow degradation rate in terms of cell-infiltration events, which is an important consideration for their subsequent application in tissue engineering. Tuning the design of these complex hydrogels by introducing proteolytic sites into the backbone of the protein has therefore been shown to improve adhesion and migration while adversely increasing hydrogel biodegradation.

These initial findings allowed us to develop a 3D-structured ELR-based hydrogel consisting of two external layers with an ELR characterized by a slow degradation rate and a central

layer containing an ELR with a fast degradation rate to achieve predetermined cell invasion, thereby improving on conventional systems in which cells infiltrate in a more random manner. Several different approaches have been explored previously to control cell migration in hydrogels, including chemotaxis, which uses biochemical stimuli incorporated into the hydrogel, or durotaxis, which usies substrate rigidity and variations in the stiffness of hydrogels to enable cells to preferentially migrate from one region of a hydrogel to another. [55] [56]

Previous studies have demonstrated that synthetic scaffolds, such as PEG hydrogels containing MMP-sensitive peptides, display promising features that can support directed and guided cell behaviour and vascularization. Additionally, other synthetic scaffolds containing collagenase-sensitive peptide sequences have been used in a variety of tissue-engineering studies.[57] [57] [58] [59] However, these peptides exhibited slow cleavage rates and their incorporation into scaffolds resulted in slow rates of degradation, thus limiting *in vivo* cell invasion, vascularization and neo-tissue formation.

The 3D-structured ELR-based hydrogels designed herein were implanted subcutaneously in mice and cellular infiltration was found to start from the central layer of the structure, which comprises the recombinamer characterized by a fast degradation rate, subsequently migrating to the external layers, which are characterized by a slow degradation rate. At six weeks post-implantation, the entire central layer of the system was completely degraded and blood vessel formation had begun, thereby facilitating the transport of nutrients. Similarly, at nine weeks post-implantation, the two sections characterized by a slow degradation rate had been completely invaded by cells and, as a result, were almost completely degraded. Finally, at 12 weeks, no signs of the 3D-structured ELR-based hydrogel were found, in other words it had been completely reabsorbed. To the best of our knowledge, the ability to control cell infiltration *in vivo* using proteolytically mediated hydrogel degradation has not been reported previously.

In light of our results, cell invasion can easily be controlled by modulating the degradation rate of biomaterials used in the engineered constructs. Moreover, the presence of proteolytic target sites with a different degradation rate may potentially lead to more rapid and enhanced infiltration in a 3D system.

5. Conclusion

Hydrogel degradation rate is a crucial aspect that must be taken into consideration when such systems are used for biomedical purposes as their utility for a specific application depends on the length of time needed for tissue repair. In this study, we have examined a spatial-temporal control of cell infiltration into a 3D-structured ELR-based hydrogel made of two specific proteolytic ELRs with different degradation rates. A pre-programmed cell infiltration that progressed via an inside-to-outside pattern was observed.

This study offers an insight into the design of a simple 3D-structured system that can be used to promote directed and guided cell migration within engineered tissues and could easily be implemented for a specific type of tissue regeneration or even for the regeneration of more biologically complex structures such as organoids or organs.

6. References

[1] Leijten J, Seo J, Yue K, Trujillo-de Santiago G, Tamayol A, Ruiz-Esparza GU, et al. Spatially and temporally controlled hydrogels for tissue engineering. Materials Science and Engineering: R: Reports. 2017;119:1-35.
[2] Drury JL, Mooney DJ. Hydrogels for tissue engineering: scaffold design variables and applications. Biomaterials. 2003;24:4337-51.
[3] Bishop ES, Mostafa S, Pakvasa M, Luu HH, Lee MJ, Wolf JM, et al. 3-D bioprinting technologies in tissue engineering and regenerative medicine: Current and future trends. Genes & diseases. 2017.
[4] Oliveira MB, Bastos HX, Mano JF. Sequentially Moldable and Bondable Four-Dimensional Hydrogels Compatible with Cell Encapsulation. Biomacromolecules. 2018.
[5] Li Y-C, Zhang YS, Akpek A, Shin SR, Khademhosseini A. 4D bioprinting: the next-generation technology for biofabrication enabled by stimuli-responsive materials. Biofabrication. 2016;9:012001.

[6] Ahearne M. Introduction to cell–hydrogel mechanosensing. Interface focus. 2014;4:20130038.

[7] Lu T, Li Y, Chen T. Techniques for fabrication and construction of three-dimensional scaffolds for tissue engineering. International journal of nanomedicine. 2013;8:337.

[8] O'brien FJ. Biomaterials & scaffolds for tissue engineering. Materials today. 2011;14:88-95.

[9] El-Sherbiny IM, Yacoub MH. Hydrogel scaffolds for tissue engineering: Progress and challenges. Global Cardiology Science and Practice. 2013:38.

[10] Hubbell JA. Biomaterials in tissue engineering. Nature Biotechnology. 1995;13:565.

[11] An J, Teoh JEM, Suntornnond R, Chua CK. Design and 3D printing of scaffolds and tissues. Engineering. 2015;1:261-8.

[12] Manavitehrani I, Fathi A, Wang Y, Maitz PK, Mirmohseni F, Cheng TL, et al. Fabrication of a Biodegradable Implant with Tunable Characteristics for Bone Implant Applications. Biomacromolecules. 2017;18:1736-46.

[13] Mahony O, Tsigkou O, Ionescu C, Minelli C, Ling L, Hanly R, et al. Silica - gelatin hybrids with tailorable degradation and mechanical properties for tissue regeneration. Advanced Functional Materials. 2010;20:3835-45.

[14] Zhang L, Liu X, Li G, Wang P, Yang Y. Tailoring degradation rates of silk fibroin scaffolds for tissue engineering. Journal of Biomedical Materials Research Part A. 2019;107:104-13.

[15] Girotti A, Reguera J, Rodríguez-Cabello JC, Arias FJ, Alonso M, Testera AM. Design and bioproduction of a recombinant multi (bio) functional elastin-like protein polymer containing cell adhesion sequences for tissue engineering purposes. Journal of Materials Science: Materials in Medicine. 2004;15:479-84.

[16] Staubli SM, Cerino G, De Torre IG, Alonso M, Oertli D, Eckstein F, et al. Control of angiogenesis and host response by modulating the cell adhesion properties of an Elastin-Like Recombinamer-based hydrogel. Biomaterials. 2017;135:30-41.

[17] Ibáñez - Fonseca A, Ramos TL, González de Torre I, Sánchez - Abarca LI, Muntión S, Arias FJ, et al. Biocompatibility of two model elastin - like recombinamer - based hydrogels formed through physical or chemical cross - linking for various applications in tissue engineering and regenerative medicine. Journal of tissue engineering and regenerative medicine. 2018;12:e1450-e60.

[18] Javier Arias F, Santos M, Fernández-Colino A, Pinedo G, Girotti A. Recent contributions of elastin-like recombinamers to biomedicine and nanotechnology. Current topics in medicinal chemistry. 2014;14:819-36.

[19] Urry DW, Parker TM, Reid MC, Gowda DC. Biocompatibility of the bioelastic materials, poly (GVGVP) and its γ-irradiation cross-linked matrix: summary of generic biological test results. Journal of Bioactive and Compatible Polymers. 1991;6:263-82.

[20] Nettles DL, Chilkoti A, Setton LA. Applications of elastin-like polypeptides in tissue engineering. Advanced drug delivery reviews. 2010;62:1479-85.

[21] MacEwan SR, Chilkoti A. Elastin - like polypeptides: Biomedical applications of tunable biopolymers. Peptide Science: Original Research on Biomolecules. 2010;94:60-77.

[22] Chan B, Leong K. Scaffolding in tissue engineering: general approaches and tissue-specific considerations. European spine journal. 2008;17:467-79.

[23] Rosso F, Giordano A, Barbarisi M, Barbarisi A. From cell–ECM interactions to tissue engineering. Journal of cellular physiology. 2004;199:174-80.

[24] Lyu S, Untereker D. Degradability of polymers for implantable biomedical devices. International journal of molecular sciences. 2009;10:4033-65.

[25] Akalp U, Bryant SJ, Vernerey FJ. Tuning tissue growth with scaffold degradation in enzyme-sensitive hydrogels: a mathematical model. Soft matter. 2016;12:7505-20.

[26] Werb Z. ECM and cell surface proteolysis: regulating cellular ecology. Cell. 1997;91:439-42.

[27] Lutolf M, Lauer-Fields J, Schmoekel H, Metters AT, Weber F, Fields G, et al. Synthetic matrix metalloproteinase-sensitive hydrogels for the conduction of tissue regeneration: engineering cell-invasion characteristics. Proceedings of the National Academy of Sciences. 2003;100:5413-8.

[28] Sokic S, Christenson M, Larson J, Appel A, Brey E, Papavasiliou G. Evaluation of MMP substrate concentration and specificity for neovascularization of hydrogel scaffolds. Biomaterials science. 2014;2:1343-54.

[29] Mecham RP, Broekelmann TJ, Fliszar CJ, Shapiro SD, Welgus HG, Senior RM. Elastin degradation by matrix metalloproteinases Cleavage site specificity and mechanisms of elastolysis. Journal of Biological Chemistry. 1997;272:18071-6.

[30] Lund LR, Green KA, Stoop AA, Ploug M, Almholt K, Lilla J, et al. Plasminogen activation independent of uPA and tPA maintains wound healing in gene - deficient mice. The EMBO journal. 2006;25:2686-97.

[31] Van Hinsbergh VW, Engelse MA, Quax PH. Pericellular proteases in angiogenesis and vasculogenesis. Arteriosclerosis, thrombosis, and vascular biology. 2006;26:716-28.

[32] Vassalli J-D, Sappino A, Belin D. The plasminogen activator/plasmin system. The Journal of clinical investigation. 1991;88:1067-72.

[33] Neurath H, Walsh KA. Role of proteolytic enzymes in biological regulation (a review). Proceedings of the National Academy of Sciences. 1976;73:3825-32.

[34] Yan Q, Dong H, Su J, Han J, Song B, Wei Q, et al. A Review of 3D Printing Technology for Medical Applications. Engineering. 2018.

[35] Banerjee A, Chatterjee K, Madras G. Enzymatic degradation of polymers: a brief review. Materials Science and Technology. 2014;30:567-73.

[36] Straley KS, Heilshorn SC. Dynamic, 3D - Pattern Formation Within Enzyme - Responsive Hydrogels. Advanced Materials. 2009;21:4148-52.

[37] Girotti A, Fernández - Colino A, López IM, Rodríguez - Cabello JC, Arias FJ. Elastin - like recombinamers: Biosynthetic strategies and biotechnological applications. Biotechnology journal. 2011;6:1174-86.

[38] Testera AM, Girotti A, de Torre IG, Quintanilla L, Santos M, Alonso M, et al. Biocompatible elastin-like click gels: design, synthesis and characterization. Journal of Materials Science: Materials in Medicine. 2015;26:105.

[39] Rodríguez-Cabello JC, Girotti A, Ribeiro A, Arias FJ. Synthesis of genetically engineered protein polymers (recombinamers) as an example of advanced self-assembled smart materials. Nanotechnology in Regenerative Medicine: Springer; 2012. p. 17-38.

[40] Fischer AH, Jacobson KA, Rose J, Zeller R. Hematoxylin and eosin staining of tissue and cell sections. Cold Spring Harbor Protocols. 2008;2008:pdb. prot4986.

[41] Ke S-H, Coombs GS, Tachias K, Corey DR, Madison EL. Optimal subsite occupancy and design of a selective inhibitor of urokinase. Journal of Biological Chemistry. 1997;272:20456-62.

[42] Vedadghavami A, Minooei F, Mohammadi MH, Khetani S, Kolahchi AR, Mashayekhan S, et al. Manufacturing of hydrogel biomaterials with controlled mechanical properties for tissue engineering applications. Acta biomaterialia. 2017;62:42-63.

[43] Hollister SJ. Porous scaffold design for tissue engineering. Nature materials. 2005;4:518.

[44] Nair LS, Laurencin CT. Biodegradable polymers as biomaterials. Progress in polymer science. 2007;32:762-98.

[45] Jammalamadaka U, Tappa K. Recent advances in biomaterials for 3D printing and tissue engineering. Journal of functional biomaterials. 2018;9:22.

[46] Khademhosseini A, Langer R. A decade of progress in tissue engineering. Nature protocols. 2016;11:1775.

[47] Miao S, Zhu W, Castro NJ, Leng J, Zhang LG. Four-dimensional printing hierarchy scaffolds with highly biocompatible smart polymers for tissue engineering applications. Tissue Engineering Part C: Methods. 2016;22:952-63.

[48] West JL, Hubbell JA. Polymeric biomaterials with degradation sites for proteases involved in cell migration. Macromolecules. 1999;32:241-4.

[49] Zhang YS, Khademhosseini A. Advances in engineering hydrogels. Science. 2017;356:eaaf3627.

[50] Coletta DJ, Ibáñez-Fonseca A, Missana LR, Jammal MV, Vitelli EJ, Aimone M, et al. Bone Regeneration Mediated by a Bioactive and Biodegradable Extracellular Matrix-Like Hydrogel Based on Elastin-Like Recombinamers. Tissue Engineering Part A. 2017;23:1361-71.

[51] Rodríguez-Cabello JC, de Torre IG, Ibañez-Fonseca A, Alonso M. Bioactive scaffolds based on elastin-like materials for wound healing. Advanced drug delivery reviews. 2018;129:118-33.

[52] de Torre IG, Ibáñez-Fonseca A, Quintanilla L, Alonso M, Rodríguez-Cabello J-C. Random and oriented electrospun fibers based on a multicomponent, in situ clickable elastin-like recombinamer system for dermal tissue engineering. Acta biomaterialia. 2018;72:137-49.

[53] Pescador D, Ibáñez-Fonseca A, Sánchez-Guijo F, Briñón JG, Arias FJ, Muntión S, et al. Regeneration of hyaline cartilage promoted by xenogeneic mesenchymal stromal cells embedded within elastin-like recombinamer-based bioactive hydrogels. Journal of Materials Science: Materials in Medicine. 2017;28:115.

[54] de Torre IG, Wolf F, Santos M, Rongen L, Alonso M, Jockenhoevel S, et al. Elastin-like recombinamer-covered stents: Towards a fully biocompatible and non-thrombogenic device for cardiovascular diseases. Acta biomaterialia. 2015;12:146-55.

[55] Sung H-J, Meredith C, Johnson C, Galis ZS. The effect of scaffold degradation rate on three-dimensional cell growth and angiogenesis. Biomaterials. 2004;25:5735-42.

[56] Azevedo HS, Reis RL. Understanding the enzymatic degradation of biodegradable polymers and strategies to control their degradation rate. Biodegradable systems in tissue engineering and regenerative medicine. 2005:177-201.

[57] Wade RJ, Bassin EJ, Rodell CB, Burdick JA. Protease-degradable electrospun fibrous hydrogels. Nature communications. 2015;6:6639.

[58] Galler KM, Aulisa L, Regan KR, D'Souza RN, Hartgerink JD. Self-assembling multidomain peptide hydrogels: designed susceptibility to enzymatic cleavage allows enhanced cell migration and spreading. Journal of the American Chemical Society. 2010;132:3217-23.

[59] Jun HW, Yuwono V, Paramonov SE, Hartgerink JD. Enzyme‐mediated degradation of peptide‐amphiphile nanofiber networks. Advanced Materials. 2005;17:2612-7.

7. Acknowledgements